Royal Society Publishing
Informing the science of the future

Incoherent Imaging of Thin Specimens Using Coherently Scattered Electrons
Author(s): D. E. Jesson and S. J. Pennycook
Source: *Proceedings: Mathematical and Physical Sciences*, Vol. 441, No. 1912 (May 8, 1993), pp. 261-281
Published by: The Royal Society
Stable URL: http://www.jstor.org/stable/52267
Accessed: 27/01/2009 12:06

Your use of the JSTOR archive indicates your acceptance of JSTOR's Terms and Conditions of Use, available at http://www.jstor.org/page/info/about/policies/terms.jsp. JSTOR's Terms and Conditions of Use provides, in part, that unless you have obtained prior permission, you may not download an entire issue of a journal or multiple copies of articles, and you may use content in the JSTOR archive only for your personal, non-commercial use.

Please contact the publisher regarding any further use of this work. Publisher contact information may be obtained at http://www.jstor.org/action/showPublisher?publisherCode=rsl.

Each copy of any part of a JSTOR transmission must contain the same copyright notice that appears on the screen or printed page of such transmission.

JSTOR is a not-for-profit organization founded in 1995 to build trusted digital archives for scholarship. We work with the scholarly community to preserve their work and the materials they rely upon, and to build a common research platform that promotes the discovery and use of these resources. For more information about JSTOR, please contact support@jstor.org.

The Royal Society is collaborating with JSTOR to digitize, preserve and extend access to *Proceedings: Mathematical and Physical Sciences.*

http://www.jstor.org

Incoherent imaging of thin specimens using coherently scattered electrons

By D. E. Jesson and S. J. Pennycook

Solid State Division, Oak Ridge National Laboratory, Oak Ridge, Tennessee 37831, U.S.A.

We consider the imaging of phase objects using a scanning transmission electron microscope equipped with a large inner-angle annular detector. We show, contrary to popular expectation, that incoherent imaging theory can be used to describe the imaging process in a plane perpendicular to the optical axis. Interference effects between atoms possessing the same projected coordinates must, however, be considered explicitly.

1. Introduction

The recent development of a powerful new technique for imaging low-index crystal projections (Pennycook & Jesson 1990, 1991) has revived considerable interest in scanning transmission electron microscopy (STEM) (Crewe 1970; Crewe & Wall 1970; Wall *et al.* 1973). Atomic resolution Z-contrast images can now be routinely obtained on a VG Microscopes HB501 UX STEM which display characteristics very close to those expected for ideal incoherent imaging. Utilizing the large inner-angle annular dark-field (ADF) detector proposed by Howie (1979), we primarily sample incoherently generated thermally scattered electrons (Hall 1965). We find that the direct interpretability and atomic number sensitivity of our images more than compensates for the associated reduction in signal-to-noise ratio. Indeed, the use of a 75 mrad inner-detector angle provides no significant practical limitation to the study of semiconductors (Jesson *et al.* 1991, 1992) and superconductors (Pennycook *et al.* 1991) over a wide range of specimen thickness (*ca.* 5–40 nm).

In the present paper, we consider the rather different conditions appropriate to the STEM imaging of very thin specimens which scatter relatively weakly to high angles. Such specimens may include heavy atoms, clusters of atoms, or extremely thin crystals which are directly relevant to many active areas of electron microscopy, including the heavy atom staining and imaging of biological materials, surface diffusion studies, and catalysis. For these objects, the intensity distribution in the STEM detector plane will be dominated by coherent scattering, and for current detector efficiencies, the inner angle of the Howie detector must be reduced to achieve an acceptable signal-to-noise ratio. The outstanding question is, therefore, under what conditions (if any) can incoherent imaging theory be applied to interpret STEM images formed primarily from coherently scattered electrons?

To quote the succinct abstract from the short note by Ade (1977), 'The assumption that images obtained in the scanning transmission electron microscope with a large annular detector may be interpreted in terms of the theory for incoherent imaging is shown to be unjustified in the case of high resolution'. The same conclusion was also reached by Cowley (1976), who pointed out that although the use of incoherent

Proc. R. Soc. Lond. A (1993) **441**, 261–281
Printed in Great Britain
© 1993 The Royal Society

imaging theory is justified in the case of well-resolved single atoms, its use may give rise to appreciable error when describing the imaging of two-dimensional clusters of atoms close to the resolution limit of the STEM instrument. The basic problem arises when atoms are separated on a scale comparable to the probe dimensions. Interference effects can appreciably modify the distribution of scattered electrons in the proximity of the central hole of the annular detector. The assumption that the dark-field signal is proportional to the total scattered radiation is then unjustified. This leads to the accepted notion that it is necessary to detect *all* of the scattered radiation to form incoherent images at atomic resolution. Reducing the detector inner angle will, therefore, improve the situation but will also require a smaller objective aperture which necessarily degrades the resolution of the imaging experiment (Ade 1977).

Thus, we arrive at the hole-in-the-detector problem which has become accepted fact in all modern articles on STEM imaging theory (Cowley 1986, 1988; Colliex & Mory 1983; Xu *et al.* 1990). It is regarded as the single obstacle preventing the direct interpretation of dark-field STEM images obtained from phase objects at atomic resolution. In this paper, we will show how to circumvent this problem using a high-angle ADF detector. We shall demonstrate in §§2–4 that, with a suitably chosen ADF detector inner angle, it is in principle possible to suppress interference effects between atoms located in a plane perpendicular to the optical axis of the microscope. Thus it is possible to obtain atomic resolution incoherent images of phase objects using coherently scattered electrons. In §5, we draw an important distinction between the transverse incoherent imaging of phase objects discussed in §2 and the imaging of three-dimensional objects. Here, we show that z-coherence effects, which involve interference between atoms located at different depths in the object, cannot be eliminated by using an ADF detector. Thus, although the images of phase objects may exhibit a transverse incoherent character, the simple interpretation of columnar intensities as a linear sum of atomic scattering cross sections can give rise to appreciable error.

2. Imaging phase objects: the hole-in-the-detector problem

Our mathematical description of STEM will emphasize a partition of the imaging process into components parallel and perpendicular to the optical axis of the microscope $\hat{z}$ (figure 1). In this way, a clear distinction can be made between the separate effects of transverse and z-coherence as discussed in §1. We, therefore, write a general positional coordinate $\boldsymbol{r}$ in the form $\boldsymbol{r} = (\boldsymbol{R}, z)$ where $\boldsymbol{R}$ is a two-dimensional (2D) real space vector perpendicular to $\hat{z}$. Likewise, we denote positions in the objective aperture and detector planes by the 2D reciprocal space vector $\boldsymbol{u}$.

Our formulation of the hole-in-the-detector problem closely follows the approaches of Cowley (1976) and Ade (1977). For a field emission source, the coherence width of the illumination at the objective aperture is considerably greater than the aperture width. To a good approximation, the probe wavefunction $P(\boldsymbol{R}-\boldsymbol{R}_0)$ for a scan coordinate $\boldsymbol{R}_0$ can be represented as a phase aberrated spherical wave;

$$P(\boldsymbol{R}-\boldsymbol{R}_0) = \mathscr{F}[A(\boldsymbol{u})\exp(\mathrm{i}\chi(\boldsymbol{u})+2\pi\mathrm{i}\boldsymbol{u}\cdot\boldsymbol{R}_0)], \tag{1}$$

where $\mathscr{F}$, here and elsewhere, denotes a Fourier transform operation. The objective aperture function

$$A(\boldsymbol{u}) = \begin{cases} 1, & \text{inside the aperture hole} \\ 0, & \text{otherwise} \end{cases}$$

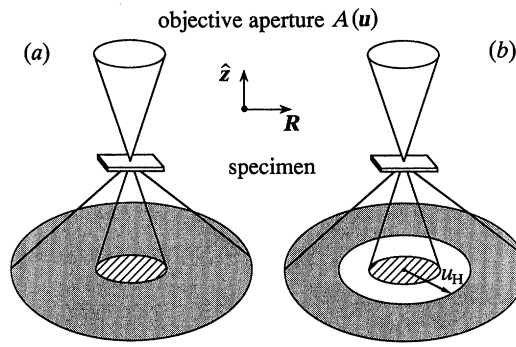

Figure 1. STEM annular dark-field imaging geometry. A small focused electron probe is scanned over the surface of a thin specimen. Simultaneously, transmitted electrons scattered through large angles are collected using an annular detector. The image is therefore built up as a function of probe position. To optimize the signal-to-noise ratio, it is customary to make the inner detector radius u_c equal to the radius of the directly transmitted disc as shown in (*a*). In (*b*), we increase the radius of the detector hole to u_H and form a Howie-type detector. The conventional and Howie-type geometries are characterized by the detector functions $D(\boldsymbol{u})$ and $D^H(\boldsymbol{u})$, respectively.

and $\chi(\boldsymbol{u})$ represents the phase perturbation for a defocus Δf and spherical aberration coefficient C_s,

$$\chi(\boldsymbol{u}) = \pi\,\Delta f\,\lambda u^2 + \tfrac{1}{2}\pi\,C_s\,\lambda^3 u^4, \tag{2}$$

where λ is the incident electron wavelength. We now assume that the specimen is sufficiently thin so that the transmittance of the probe can be described by a multiplicative transmission function. For purely elastic scattering, the scattered electron wave at the exit surface of the specimen may be written

$$\psi(\boldsymbol{R}-\boldsymbol{R}_o) = P(\boldsymbol{R}-\boldsymbol{R}_o)\exp(-\mathrm{i}\sigma\phi(\boldsymbol{R})). \tag{3}$$

This is the phase object approximation (POA). Absorption can be included explicitly in (3) but is small for very thin specimens and is subsequently ignored in this analysis. It is assumed that the phase change of the probe wavefunction is proportional to the projected potential

$$\phi(\boldsymbol{R}) = \int \phi(\boldsymbol{r})\,\mathrm{d}z, \tag{4}$$

where the interaction constant $\sigma = \pi/\lambda E$ and E is the accelerating voltage. Thus Fresnel diffraction is ignored, which is equivalent to assuming a flat Ewald sphere. The convenient idea of imaging a phase object with an inner detector angle θ_i is therefore limited to specimens somewhat thinner than

$$t = 2\lambda/\theta_i^2. \tag{5}$$

In practice, this gives a maximum thickness limit of around 4 nm for $\theta = 40$ mrad so that (3) is applicable to the special class of very thin specimens mentioned in the introduction over a wide range of inner-detector angles. At this point, it is customary to expand the exponential in (3) and truncate the series to a given power in $\sigma\phi(\boldsymbol{R})$. For the sake of clarity, we follow this convention here and ignore all terms higher than second order giving;

$$\psi(\boldsymbol{R}-\boldsymbol{R}_o) = P(\boldsymbol{R}-\boldsymbol{R}_o) - \mathrm{i}\sigma\phi(\boldsymbol{R})P(\boldsymbol{R}-\boldsymbol{R}_o) - \tfrac{1}{2}\sigma^2\phi^2(\boldsymbol{R})P(\boldsymbol{R}-\boldsymbol{R}_o). \tag{6}$$

The neglect of higher-order terms in this expression for strongly scattering objects

may not be valid and will be considered later. Within the second-order approximation, the wave amplitude in the detector plane is given by the Fourier transform of (6):

$$\Psi(\boldsymbol{u}) = A(\boldsymbol{u})\exp(\mathrm{i}\chi(\boldsymbol{u})+2\pi\mathrm{i}\boldsymbol{u}\cdot\boldsymbol{R}_0)-\mathrm{i}\sigma\Phi(\boldsymbol{u})*A(\boldsymbol{u})\exp(\mathrm{i}\chi(\boldsymbol{u})+2\pi\mathrm{i}\boldsymbol{u}\cdot\boldsymbol{R}_0) -\tfrac{1}{2}\sigma^2\Phi(\boldsymbol{u})*\Phi(\boldsymbol{u})*A(\boldsymbol{u})\exp(\mathrm{i}\chi(\boldsymbol{u})+2\pi\mathrm{i}\boldsymbol{u}\cdot\boldsymbol{R}_0), \quad (7)$$

where $\Phi(\boldsymbol{u})$ is the Fourier transform of $\phi(\boldsymbol{R})$. The intensity in the diffraction plane (to second order in $\sigma\Phi(\boldsymbol{u})$) becomes

$$|\Psi(\boldsymbol{u})|^2 = A^2(\boldsymbol{u})+2\sigma Re\{A(\boldsymbol{u})\exp(\mathrm{i}\chi(\boldsymbol{u})+2\pi\mathrm{i}\boldsymbol{u}\cdot\boldsymbol{R}_0)[\mathrm{i}\Phi^*(\boldsymbol{u})*A(\boldsymbol{u})\exp(-\mathrm{i}\chi(\boldsymbol{u}) -2\pi\mathrm{i}\boldsymbol{u}\cdot\boldsymbol{R}_0)-\tfrac{1}{2}\sigma\,\Phi^*(\boldsymbol{u})*\Phi^*(\boldsymbol{u})*A(\boldsymbol{u})\exp(-\mathrm{i}\chi(\boldsymbol{u}) -2\pi\mathrm{i}\boldsymbol{u}\cdot\boldsymbol{R}_0)]\}+\sigma^2|\Phi(\boldsymbol{u})*A(\boldsymbol{u})\exp(\mathrm{i}\chi(\boldsymbol{u})+2\pi\mathrm{i}\boldsymbol{u}\cdot\boldsymbol{R}_0)|^2. \quad (8)$$

The first term of (8) simply represents a central disc of intensity formed by directly transmitted electrons. The second and third terms contained in square brackets are both multiplied by $A(\boldsymbol{u})$ and so represent intensity modulations within this disc. Only the fourth term extends beyond the central disc and contributes to the STEM dark-field signal $I(\boldsymbol{R}_0)$ given by

$$I(\boldsymbol{R}_0) = \int|\Psi(\boldsymbol{u})|^2 D(\boldsymbol{u})\,\mathrm{d}\boldsymbol{u}. \quad (9)$$

Without introducing significant error, the ADF detector function $D(\boldsymbol{u})$ is written as

$$D(\boldsymbol{u}) = \begin{cases}1, & \text{if } |\boldsymbol{u}| > u_c,\\ 0, & \text{otherwise.}\end{cases} \quad (10)$$

This corresponds to an infinite outer detector angle which is justified in practice by the rapid fall-off in signal with scattering angle θ. If the inner detector angle (of radius u_c) exactly corresponds to the probe convergence angle, we have

$$D(\boldsymbol{u}) = 1-A(\boldsymbol{u}), \quad (11)$$

which is the condition usually assumed for conventional ADF STEM imaging. Substituting (8) and (11) into (9) gives the image intensity as

$$I(\boldsymbol{R}_0) = \sigma^2\int|\Phi(\boldsymbol{u})*A(\boldsymbol{u})\exp\{\mathrm{i}\chi(\boldsymbol{u})+2\pi\mathrm{i}\boldsymbol{u}\cdot\boldsymbol{R}_0\}|^2\,\mathrm{d}\boldsymbol{u} -\sigma^2\int A(\boldsymbol{u})|\Phi(\boldsymbol{u})*A(\boldsymbol{u})\exp\{\mathrm{i}\chi(\boldsymbol{u})+2\pi\mathrm{i}\boldsymbol{u}\cdot\boldsymbol{R}_0\}|^2\,\mathrm{d}\boldsymbol{u}. \quad (12)$$

Equation (12) is identical to (29) of Cowley (1976) and (11) of Ade (1977). It is the standard expression used to consider the hole-in-the-detector problem and is reproduced for this purpose in many recent review articles (Cowley 1986, 1988; Colliex & Mory 1983). To obtain linear incoherent imaging of the function $\sigma^2\phi^2(\boldsymbol{R})$, it is necessary to assume that the second integral in (12) is either zero or proportional to the first integral. Physically, this requires the dark-field signal to equal the total scattered radiation or a constant fraction of it. It is generally assumed that this can only be achieved by reducing the hole in the detector until the second term is insignificant, giving,

$$I(\boldsymbol{R}_0) = \sigma^2\int|\phi(\boldsymbol{R})P(\boldsymbol{R}-\boldsymbol{R}_0)|^2\,\mathrm{d}\boldsymbol{R} = \sigma^2\phi^2(\boldsymbol{R}_0)*P^2(\boldsymbol{R}_0). \quad (13)$$

This is the standard optical equation for incoherent imaging (Goodman 1968) where $P^2(\boldsymbol{R}-\boldsymbol{R}_0)$ is the surface probe intensity profile. The accepted belief is that this result will break down near the resolution limit of the STEM instrument (Ade 1977; Cowley 1976, 1986, 1988; Colliex & Mory 1983; Xu *et al.* 1990) when oscillations of $\Phi(\boldsymbol{u})$ are on a scale comparable with the hole in the detector. The two integrals in (12) will then not be proportional, and it is argued that incoherent imaging theory is inapplicable at atomic resolution.

We now re-examine the hole-in-the-detector argument of §2 from a new perspective. Consider replacing the standard ADF detector function $D(\boldsymbol{u})$ (equation (11)) by the Howie detector function $D^{\mathrm{H}}(\boldsymbol{u})$ so that

$$D^{\mathrm{H}}(\boldsymbol{u}) = \begin{cases} 1, & \text{for } |\boldsymbol{u}| > u_{\mathrm{H}}, \\ 0, & \text{otherwise}, \end{cases} \tag{14}$$

where u_{H} is the adjustable inner detector radius. The modified dark-field signal is from (12);

$$I(\boldsymbol{R}_0) = \sigma^2 \int |\Phi(\boldsymbol{u}) * A(\boldsymbol{u}) \exp(\mathrm{i}\chi(\boldsymbol{u}) + 2\pi \mathrm{i}\boldsymbol{u}\cdot\boldsymbol{R}_0)|^2 D^{\mathrm{H}}(\boldsymbol{u})\,\mathrm{d}\boldsymbol{u}, \tag{15}$$

which for a phase insensitive detector can be written

$$I(\boldsymbol{R}_0) = \sigma^2 \int |[\Phi(\boldsymbol{u}) * A(\boldsymbol{u}) \exp(\mathrm{i}\chi(\boldsymbol{u}) + 2\pi \mathrm{i}\boldsymbol{u}\cdot\boldsymbol{R}_0)] D^{\mathrm{H}}(\boldsymbol{u})|^2\,\mathrm{d}\boldsymbol{u}. \tag{16}$$

Parseval's Theorem, exploiting the conservation of energy in real and reciprocal space for a restricted range of spatial frequencies, then gives

$$I(\boldsymbol{R}_0) = \sigma^2 \int |\phi(\boldsymbol{R})\, P(\boldsymbol{R}-\boldsymbol{R}_0) * d(\boldsymbol{R})|^2\,\mathrm{d}\boldsymbol{R}, \tag{17}$$

where $d(\boldsymbol{R})$ is the spatial frequency filter

$$d(\boldsymbol{R}) = \mathscr{F}[D^{\mathrm{H}}(\boldsymbol{u})] = \delta(\boldsymbol{R}) - u_{\mathrm{H}} J_1(2\pi u_{\mathrm{H}} R)/R. \tag{18}$$

Equations (17) and (15) represent our basic results describing the STEM dark-field imaging of phase objects to second order in $\sigma\phi(\boldsymbol{R})$. To extend the analysis beyond this point, we must now consider the nature of the object in more detail. Single atoms, 2D atomic clusters, and low-index crystal projections are all examples of special objects associated with potentials which are sharply peaked at the atom sites. To a good approximation, it is possible to describe the phase object as a sum of projected atomic contributions so that

$$\phi(\boldsymbol{R}) = \sum_i \phi_i(\boldsymbol{R}-\boldsymbol{R}_i), \tag{19}$$

where

$$\phi_i(\boldsymbol{R}) = \int \phi_i(\boldsymbol{r})\,\mathrm{d}z \tag{20}$$

is a potential function describing the ith atom located at $\boldsymbol{R}_i$ (note more than one atom can have the same projected coordinate $\boldsymbol{R}_i$). We can now write the real space expression (equation (17)) for the dark-field signal as

$$I(\boldsymbol{R}_0) = \sigma^2 \int \left| \sum_i \phi_i(\boldsymbol{R}-\boldsymbol{R}_i)\, P(\boldsymbol{R}-\boldsymbol{R}_0) * d(\boldsymbol{R}) \right|^2 \mathrm{d}\boldsymbol{R}. \tag{21}$$

Utilizing the *a priori* information that the $\phi_i(\boldsymbol{R}-\boldsymbol{R}_i)$ are sharply peaked about the sites $\boldsymbol{R}_i$, we are now in a position to analyse the integrand of (21) further and present general arguments leading to the idea of transverse incoherence. Such arguments will be considered more quantitatively in §3.

By increasing the inner radius u_{i} of the annular detector so that

$$u_{\mathrm{H}} \gg 1/\Delta P, \tag{22}$$

it is always possible to make $d(\boldsymbol{R})$ narrow on the scale of the probe amplitude function of width ΔP. To a good approximation, the probe will then only act as a scaling factor in real space for the range of spatial frequencies in $\phi_i(\boldsymbol{R}-\boldsymbol{R}_i)$ which are selected by the annular detector. This means we can justifiably remove the probe from the convolution in the integrand and rewrite (21) in the form,

$$I(\boldsymbol{R}_{\mathrm{o}}) = \sigma^2 \int \left| \sum_i [\phi_i(\boldsymbol{R}-\boldsymbol{R}_i) * d(\boldsymbol{R})] P(\boldsymbol{R}-\boldsymbol{R}_{\mathrm{o}}) \right|^2 \mathrm{d}\boldsymbol{R} = P^2(\boldsymbol{R}_{\mathrm{o}}) * O(\boldsymbol{R}_{\mathrm{o}}), \tag{23}$$

where $O(\boldsymbol{R})$ is a characteristic specimen object function;

$$O(\boldsymbol{R}) = \sigma^2 \left| \sum_{\boldsymbol{R}_i} n_i \phi_i(\boldsymbol{R}_i) * d(\boldsymbol{R}) \right|^2 \tag{24}$$

and n_i is the number of atoms in the ith column. Equation (23) is an important result indicating that incoherent imaging theory is indeed applicable to the dark-field STEM imaging of phase objects at atomic resolution. However, at this point we have incoherent imaging of an object function which is a coherent superposition of spatially filtered columnar functions. This means that individual columns do not scatter independently so that it is difficult to intuitively interpret the image in terms of scattering powers although the linear incoherent imaging of $O(\boldsymbol{R})$, as suggested by (23), still conveys a number of distinct advantages over equivalent coherent imaging methods. These include the elimination of image artefacts with defocus, since it is known for incoherent imaging that only one optimum contrast defocus condition exists. Thus images may be interpreted with an intrinsically better interpretable resolution limit given by the Scherzer condition for incoherent imaging ($\Delta f = -\sqrt{(\lambda C_{\mathrm{s}})}$ (Scherzer 1949)) which corresponds to the most compact surface probe intensity profile (Pennycook & Jesson 1991).

In the special case of well-separated single atoms, the atomic contributions to the object function (equation (24)) do not overlap, and (23) implies incoherent imaging of each atom. Note, however, that it is still necessary to satisfy (22) to obtain an incoherent image of isolated atoms. In a conventional STEM geometry, which does not satisfy (22), the dark-field signal is dominated by relatively low-angle scattering where the probe and the atom potential vary on the same scale. Thus an image of a single atom will not in general map the probe intensity profile. An incoherent result is therefore only approached at low resolution when the scattering down the detector hole is negligible (equation (13)).

For more general phase objects, we now introduce a further level of incoherence into the imaging process by ensuring that

$$u_{\mathrm{H}} \gg 1/\Delta R, \tag{25}$$

where ΔR is the separation between peaks in the object function. The spatially filtered columnar functions become progressively narrower as u_{H} is increased with

the result that, eventually, the atomic contributions to $O(\boldsymbol{R})$ from different columns no longer overlap. Equation (25) therefore defines the condition required to obtain incoherent scattering from individual atomic columns. The object function is then expressible in terms of independent contributions;

$$O(\boldsymbol{R}) = \sigma^2 \sum_{\boldsymbol{R}_i} O_i(\boldsymbol{R}-\boldsymbol{R}_i), \tag{26}$$

where

$$O_i(\boldsymbol{R}) = |n_i \phi_i(\boldsymbol{R}_i) * d(\boldsymbol{R})|^2 \approx \delta(\boldsymbol{R}-\boldsymbol{R}_i) \int O_i(\boldsymbol{R})\,\mathrm{d}\boldsymbol{R}$$

$$= \delta(\boldsymbol{R}-\boldsymbol{R}_i) \int n_i^2 \Phi_i^2(\boldsymbol{u}) D^{\mathrm{H}}(\boldsymbol{u})\,\mathrm{d}\boldsymbol{u}. \tag{27}$$

$\Phi_i(\boldsymbol{u})$ is the Fourier transform of $\phi_i(\boldsymbol{R})$ so that the object function is close to a set of delta functions located at the sites $\boldsymbol{R}_i$ and weighted with the relevant atomic cross sections for scattering to the high-angle detector. Thus we now have a 2D object function composed of independent scatterers. $O(\boldsymbol{R})$ represents an intuitively interpretable map of the specimen scattering power which assumes a greater sensitivity to atomic number as u_{H} is increased. The linear incoherent imaging of this function offered by (23) therefore conveys the clear potential to interpret the image intuitively in terms of columnar scattering powers. We define this capability of the imaging geometry to eliminate interference effects between columns as transverse incoherence.

Consider, however, the contribution of one or more atoms having the same projected coordinate $\boldsymbol{R}_i$ and which form a column along the z-direction. Equations (23)–(27) suggest that the corresponding peak in $O(\boldsymbol{R})$ will be imaged with a strength proportional to the square of the number of atoms in a column, and this in turn will be modified further for strong phase objects. The peak is not simply an incoherent sum of scattering cross sections. We collectively refer to such interferences which cannot be eliminated by a Howie detector as resulting from z-coherence effects (see §5). The connection between (22) and incoherent imaging was noted previously by Engel (1974*a*, *b*). However, he did not consider the spacings in the object (equation (25)) or the effects of z-coherence on the image.

3. Transverse incoherent imaging of atomic clusters

In this section, we begin our quantitative study of the ideas developed in §2 by considering the imaging of two atoms. We shall find that this simple problem clearly illustrates the important ideas applicable to more elaborate arrangements of atoms. For a phase object consisting of two identical atoms located at $\boldsymbol{R}_1$ and $\boldsymbol{R}_2$, the integrand of (21), which corresponds to the total scattering, is given by

$$I(\boldsymbol{R}, \boldsymbol{R}_0) = \sigma^2 |[\phi_{\mathrm{A}}(\boldsymbol{R}) * (\delta(\boldsymbol{R}-\boldsymbol{R}_1) + \delta(\boldsymbol{R}-\boldsymbol{R}_2))] P(\boldsymbol{R}-\boldsymbol{R}_0)|^2. \tag{28}$$

If the atomic potential $\phi_{\mathrm{A}}(\boldsymbol{R})$ is considerably sharper than the probe amplitude profile $P(\boldsymbol{R}-\boldsymbol{R}_0)$, then from Parsevals theorem the intensity distribution in the detector plane becomes

$$I(\boldsymbol{u}, \boldsymbol{R}_0) = \sigma^2 \Phi_{\mathrm{A}}^2(\boldsymbol{u}) [P^2(\boldsymbol{R}_0-\boldsymbol{R}_1) + P^2(\boldsymbol{R}_0-\boldsymbol{R}_2) + 2\,Re\{P(\boldsymbol{R}_0-\boldsymbol{R}_1) P^*(\boldsymbol{R}_0-\boldsymbol{R}_2) \cos[\Delta\boldsymbol{R}\cdot\boldsymbol{u}]\}], \tag{29}$$

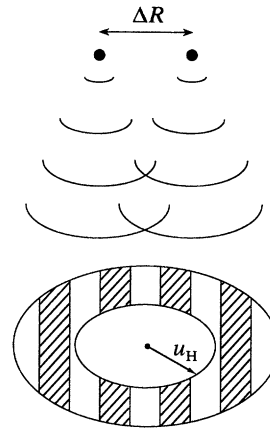

Figure 2. The equivalence of the STEM ADF scattering geometry to the interference pattern produced at the Howie detector by two point sources separated by a distance ΔR (see text).

where $\Delta \boldsymbol{R} = \boldsymbol{R}_1 - \boldsymbol{R}_2$ defines the atomic separation and $\Phi_A(\boldsymbol{u})$ is the atomic scattering factor. In this expression we have neglected terms in $\sin(\Delta \boldsymbol{R} \cdot \boldsymbol{u})$ which would cancel upon integration over the ADF detector. Essentially therefore, the intensity distribution defined by (29) is equivalent to the interference pattern produced by two point sources of strength $P(\boldsymbol{R}-\boldsymbol{R}_1)\,\Phi_A(\boldsymbol{u})$ and $P(\boldsymbol{R}-\boldsymbol{R}_2)\,\Phi_A(\boldsymbol{u})$ located at the atom positions (figure 2).

Clearly, the intensity distribution from the two atoms scattering incoherently is given by

$$I^{\mathrm{inc}}(\boldsymbol{u}, \boldsymbol{R}_0) = \sigma^2 \Phi_A^2(\boldsymbol{u})\,[P^2(\boldsymbol{R}_0-\boldsymbol{R}_1)+P^2(\boldsymbol{R}_0-\boldsymbol{R}_2)], \tag{30}$$

which is simply the probe intensity at the atom sites multiplied by the relevant scattering cross section. Therefore, the ratio of the detected signal to the ideal incoherent signal for an ADF detector of inner radius u_i is given by

$$R(u_i, \boldsymbol{R}_0) = 1 + \frac{2\,Re\,[P(\boldsymbol{R}_0-\boldsymbol{R}_1)\,P^*(\boldsymbol{R}_0-\boldsymbol{R}_2)]}{[P^2(\boldsymbol{R}_0-\boldsymbol{R}_1)+P^2(\boldsymbol{R}_0-\boldsymbol{R}_2)]}\,\xi(u_i, \Delta R), \tag{31}$$

where

$$\xi(u_i, \Delta R) = \int_{u_i}^{\infty} \Phi_A^2(\boldsymbol{u})\, u J_0(u\,\Delta R)\,\mathrm{d}u \Big/ \int_{u_i}^{\infty} u \Phi_A^2(\boldsymbol{u})\,\mathrm{d}u \tag{32}$$

expresses the deviation away from ideal incoherent imaging. In an optical sense, $\xi(u_i, \Delta R)$ can be interpreted as the real part of the complex degree of coherence γ and likewise $R(u_i, \boldsymbol{R}_0) = 1/(1-|\gamma|)$ (Born & Wolf 1980, pp. 491–555). Clearly, perfect constructive interference will result in the coherent limit where $\xi(u_i, \Delta R) = 1$ so that $R(u_i, \boldsymbol{R}_0) = 2$. This will occur for all u_i and $\boldsymbol{R}_0$ when $\Delta R = 0$ and the two coincident atoms add perfectly in phase, producing twice as much scattering as two independent scatterers over the entire angular range (figure 3*a*, *b*).

The incoherent limit $\xi(u_i, \Delta R) \to 0, R(u_i, \boldsymbol{R}_0) \to 1$ is approached when the atomic separation ΔR is very much greater than the atom size (figure 3*c*). Many phases are sampled automatically, even for relatively low-angle ADF detectors, and the detected signal is the same for two isolated atoms scattering independently. However, in many cases of practical significance, atomic potentials do overlap, and it is important to appreciate that even if *all* of the scattered radiation was detected, the signal would not be equivalent to the result expected for independent scatterers. Consider, for

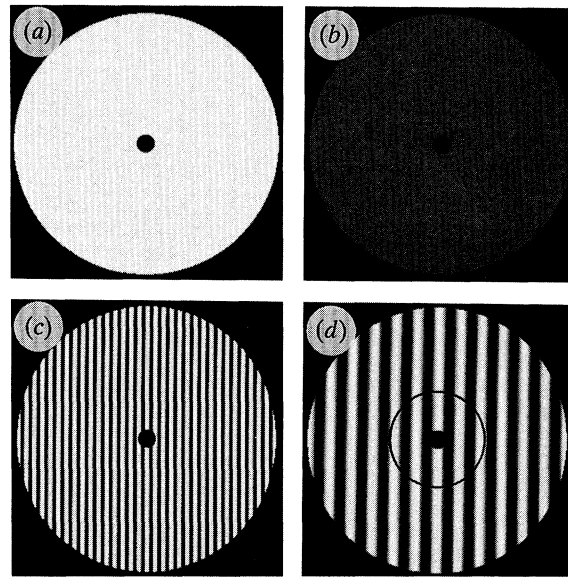

Figure 3. Detector plane intensity distribution corrsponding to the two point sources represented in figure 2. The detector inner and outer angles are 10.3 and 150 mrad, respectively. The scattering factor dependence is intentionally removed from the distributions to emphasize interference effects between atoms. In (*a*) we show the coherent limit for coincident atoms ($\Delta R = 0$), and (*b*) represents the incoherent limit corresponding to independent scatterers. The intensity distribution in (*c*) displays the fine scale interference fringes associated with well-separated atoms ($\Delta R = 3$ Å). In (*d*) $\Delta R = 1.5$ Å, and the superimposed circle shows how an increased inner detector angle of 50 mrad samples more interference fringes at the detector periphery. The operating voltage is 100 kV.

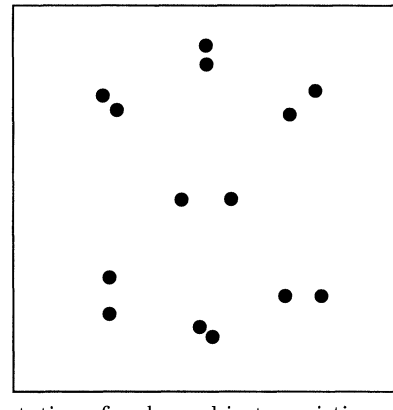

Figure 4. A schematic representation of a phase object consisting of well-separated pairs of atoms. Each solid circle represents a single atom. The probe cannot resolve individual atoms but can resolve atom pairs.

example, a phase object consisting of well-separated pairs of atoms as shown schematically in figure 4. If a small hole in the detector (corresponding to low resolution) is used to collect almost all of the scattered intensity from this object or, alternatively, the condition given by (22) is fulfilled, then the image will consist of an array of bright spots corresponding to each unresolved atom pair. In principle, such an image can, of course, be interpreted using incoherent imaging theory via (13)

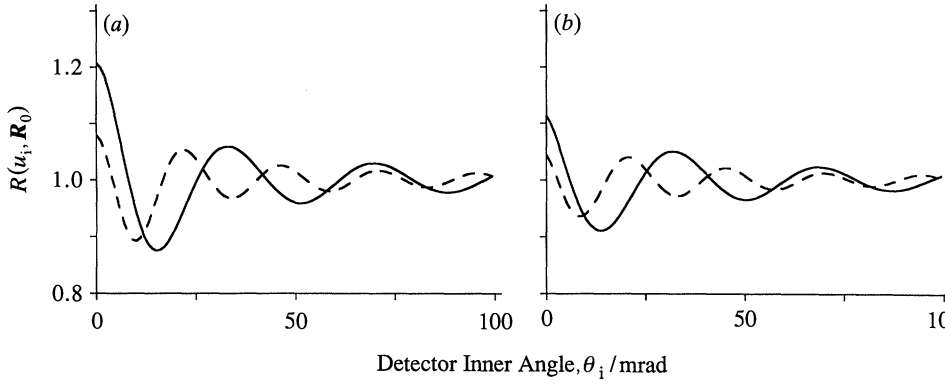

Figure 5. Ratio of the ADF signal to the incoherent signal from (*a*) two silicon and (*b*) two uranium atoms separated by 1.0 Å (solid line) and 1.5 Å (dashed line) as a function of inner detector angle θ_i. The 2.2 Å (FWHM) probe is located over the centre of the two atoms at a defocus of −70 nm. The convergence angle is 10.3 mrad and $C_s = 1.3$ mm.

or (23). However, the brightness of the spots will depend critically on the atomic separation for closely spaced pairs (equation (13) or (24)). Thus it is quite possible to confuse a pair of closely spaced atoms, for example, with three more widely separated atoms or indeed a single heavy atom.

Clearly, what is needed to remove such ambiguity is to approach the incoherent object function result (equations (26) and (27)) by increasing the inner detector angle θ_i. In figure 5*a*, we plot $\boldsymbol{R}(u_i, \boldsymbol{R}_0)$ (equation (31)) as a function of θ_i for two silicon atoms separated by 1.0 and 1.5 Å.† For small θ_i there is significant departure from incoherent imaging due to the atomic overlap effects noted earlier. In particular, the signal obtained for a 1.0 Å separation is 20% higher than the incoherent signal. By increasing the inner detector angle to 50 mrad, this is reduced to less than 5%. Similar results are obtained for uranium atom pairs as shown in figure 5*b*. Physically, this improvement is related to sampling many more interference fringes around the detector periphery as suggested by the circle in figure 3*d*. In addition, $\Phi_A^2(\boldsymbol{u})$ falls off less rapidly with increasing u so that more fringes are also averaged across the detector. In real space, increasing u_i improves the localization of the object function at the atomic sites, thus reducing interference effects between neighbouring atoms. A useful criterion for establishing incoherent imaging is when the first minima in $d(\boldsymbol{R})$ coincide for two point scatterers separated by a distance ΔR. This gives the minimum detector angle θ_i^{inc} for incoherent imaging as

$$\theta_i^{\mathrm{inc}} = 1.22\lambda/\Delta R, \tag{33}$$

which corresponds to the second minima in figure 5. Note that the detector 'resolution' criterion used to derive (33) is rather severe when compared with the Rayleigh condition applied to coherent imaging ($\theta_i^{\mathrm{coh}} = 0.82\lambda/\Delta R$) (Born & Wolf 1980, p. 424) since to obtain an incoherent signal, the peaks must be well resolved. Under these conditions, the coherent signal will deviate from the incoherent signal by about 5%. Thus, for a given atomic spacing, it is possible to adjust the detector angle using (33) to obtain an incoherent image with an optimum signal-to-noise ratio.

The extension of these ideas to the study of 2D atomic clusters involves only a straightforward extension of the object function approach for atomic pairs. However,

† 1 Å = 10^{-10} m.

some care should be directed towards situations where more than two atoms may be in close proximity in which case it may be prudent to adopt a more conservative condition than (33) for a given ΔR.

4. Transverse incoherent imaging of crystal projections

Within the limitations of the POA, the essential differences between clusters of single atoms and periodic arrangements of atomic columns become rather trivial. Consider, for example, a simple projected potential consisting of a square projected unit cell of side 4 Å containing two closely spaced atomic columns separated by 0.5 Å as shown in figure 6. With a 2.2 Å (FWHM) probe, typical of current ultrahigh resolution STEMS (Pennycook & Jesson 1990), the columnar spacing will clearly not be resolved although groups of two columns comprising a single dumbbell can be imaged individually. The situation is, therefore, directly analogous to the imaging of atomic pairs in §3.

In order to meet the criterion for a phase object, (5) limits the crystal thickness to around 3 nm for a maximum relevant scattering angle of 50 mrad. A further restriction is placed on the columnar atomic density if the analysis is limited to second-order terms in $\sigma\phi(\boldsymbol{R})$ as in §2. However, we shall show in §5 that higher-order terms do not affect the main conclusions regarding transverse incoherence so that without losing generality, we shall continue to assume a weakly scattering phase object. Then, for columns consisting of n_{Si} silicon atoms of atomic scattering factor $\Phi_{\mathrm{Si}}(u)$ located at $\boldsymbol{R}_{\mathrm{i}}$, (15) gives the image intensity as

$$\begin{aligned} I(\boldsymbol{R}_{\mathrm{o}}) = \sigma^2 \int \Bigg| \sum_{\boldsymbol{G}} \delta(\boldsymbol{u}-\boldsymbol{G}) \sum_i \Phi_i(\boldsymbol{u}) \exp(2\pi \mathrm{i}\boldsymbol{u}\cdot\boldsymbol{R}_i) * A(\boldsymbol{u}) \exp(\mathrm{i}\chi(\boldsymbol{u}) \\ + 2\pi\mathrm{i}\boldsymbol{u}\cdot\boldsymbol{R}_{\mathrm{o}}) \Bigg|^2 D^{\mathrm{H}}(\boldsymbol{u})\,\mathrm{d}\boldsymbol{u} = \sigma^2 \int \Bigg| \sum_{\boldsymbol{G}} \delta(\boldsymbol{u}-\boldsymbol{G})\, n_{\mathrm{Si}}\, \Phi_{\mathrm{Si}}(\boldsymbol{u}) [1+\exp(\tfrac{1}{8}\pi\mathrm{i}G_x)] \\ * A(\boldsymbol{u}) \exp(\mathrm{i}\chi(\boldsymbol{u}) + 2\pi\mathrm{i}\boldsymbol{u}\cdot\boldsymbol{R}_{\mathrm{o}}) \Bigg|^2 D^{\mathrm{H}}(\boldsymbol{u})\,\mathrm{d}\boldsymbol{u}. \end{aligned} \tag{34}$$

Here, the set of vectors $\{\boldsymbol{G}\}$ defines the 2D reciprocal lattice, and G_x is the component of a given $\boldsymbol{G}$ parallel to the dumbbell direction (see figure 6). The integrand in (34) represents the scattered intensity distribution on the STEM ADF detector, which for a periodic object is a coherent convergent beam electron diffraction (CBED) pattern (Zeitler & Thomson 1970; Spence & Cowley 1978). The pattern in figure 7*a* corresponds to the disc overlap geometry in figure 7*b* with the probe located at the centre of the unit cell. We have intentionally removed the angular dependence of the atomic scattering factors $\Phi_{\mathrm{Si}}(\boldsymbol{u})$ in figure 7*c* to emphasize the interference effects between different columns in the projection. This is manifested by the horizontal modulations in scattered intensity which correspond directly to the square bracketed term in (34).

The hole in the conventional ADF STEM detector shown in figure 7 exactly corresponds to the size of the directly transmitted disc and is completely located within a bright interference fringe. The dark-field signal is generally dominated by scattering closest to the hole in the detector because of the angular fall-off in the scattering factors $\Phi_{\mathrm{Si}}(\boldsymbol{u})$. Therefore, scattering from the unresolved columns at the

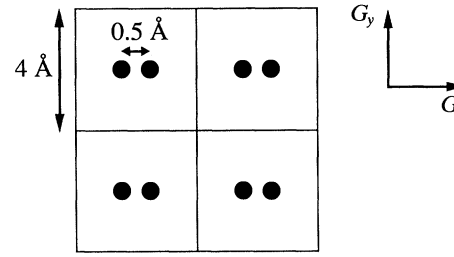

Figure 6. A simple 'two-string' crystal projection in which two closely spaced atomic columns are located in a square projected unit cell. G_x and G_y, respectively, denote components of a reciprocal lattice vector $\boldsymbol{G}$ which are parallel and perpendicular to the dumbbell direction.

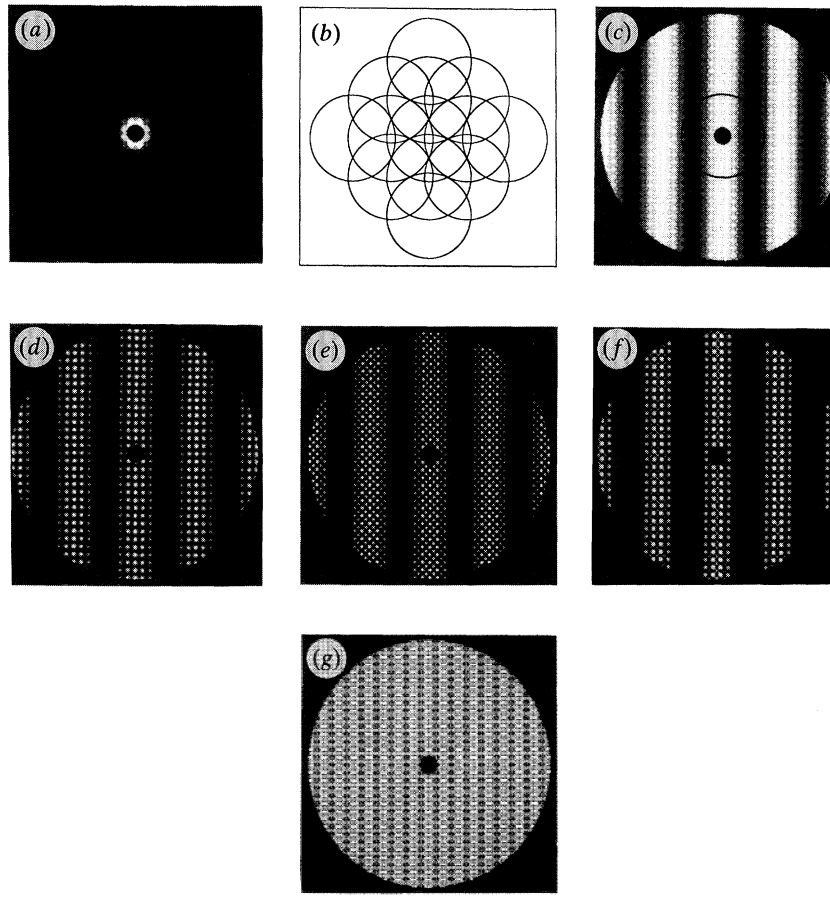

Figure 7. Calculated CBED patterns for the two-string potential contained in figure 6. The probe is located over a dumbbell in (*a*), and the geometry of the disc overlap regions is shown schematically in (*b*). The convergence angle is 10.3 mrad, and $C_s = 1.3$ mm in all simulations. The defocus is -70 nm unless stated otherwise. From (*c*) onwards, we remove the atomic scattering factor dependence to emphasize the interference effects between different atomic columns. The superimposed circle in (*c*) represents the inner radius of a 50 mrad Howie detector. The probe is located over a channel in (*d*), and in (*e*) and (*f*), the probe (over a dumbbell) is defocused to -130 and -30 nm, respectively, producing regions of destructive interference in the patterns. In (*g*), the probe is located directly over an atom with the columns of the two-string potential of figure 6 now separated by 2 Å. In all cases, the annular detector conforms to the conventional geometry represented in figure 1*a*, which ranges from 10.3 to 150 mrad. The operating voltage is 100 kV.

centre of the unit cell will tend to contribute in phase to $I(\boldsymbol{R}_0)$. As pointed out by Cowley (1976), this can produce an appreciable difference from the signal anticipated from the two columns scattering incoherently. However, it is immediately apparent from figure 7*c* that by choosing a large inner detector radius, which is significantly greater than the structure factor modulation period, many fringes will be sampled around the circumference of the hole. This will negate interference effects between columns and the signal will start to approach the incoherent cross section for each string imaged separately (Jesson & Pennycook 1990). In this rather extreme case involving closely separated strings, the error, assuming incoherent imaging, is reduced from 50% at small u_i to less than 10% for a 70 mrad inner detector angle (figure 8).

Thus we now have a clear reciprocal space interpretation of transverse incoherence, which is entirely complimentary to the real space viewpoint of §2. In particular, it is instructive to relate the image characteristics predicted by the intuitive real space analysis to the behaviour of a coherent CBED pattern. For example, the convolution of (23) clearly indicates why more intensity is scattered to the Howie detector with the probe over a dumbbell than with the probe over a channel. Figure 7*c* and *d* show the corresponding CBED patterns for these two situations. The overlapping regions of the CBED discs add in phase with the probe over the dumbbell, but interfere destructively with the probe over the channel. The real space and reciprocal space viewpoints are, therefore, entirely consistent. In a similar way, the defocus dependence of the image can be understood in real space in terms of the surface probe intensity profile. The most compact optimum defocus condition ($\Delta f = \sqrt{(\lambda C_s)}$ (Scherzer 1949)) corresponds in reciprocal space to the condition for maximum constructive interference of the CBED discs (figure 7*c*). Defocusing the probe produces regions of destructive interference in the overlap regions (figure 7*e* and *f*) which corresponds to the spreading of the probe in real space. The physical origin and justification of the real space convolution in (23), therefore, arises from the scale of interference effects in the CBED pattern formed at the detector plane. Interference fringes become more closely spaced as the columnar spacing increases (figure 7*g*). For well-resolved columns, the radius of the directly transmitted disc and hence the detector hole radius must always be considerably larger than the scale of the fringes resulting from interference between columns. This is similar to the case of well-resolved single atoms shown in figure 3*c*. Thus, many fringes are automatically sampled, even for an ADF detector $D^{\mathrm{H}}(\boldsymbol{u})$ with a relatively low inner angle. For well-resolved columns of atoms, the condition of (25) is therefore fulfilled automatically so that it is only necessary to satisfy (22) to obtain an incoherent image.

Finally, we emphasize that the ideas of transverse incoherence also apply equally well to imaging defects. Although the resulting CBED pattern from a non-periodic object is necessarily more complicated, identical considerations still apply to the elimination of interference effects between a random array of columns (see, for example, the discussion of atomic clusters in §3). Indeed, the concept of a coherence volume, elongated in the z-direction, is clearly evident from the elimination of speckle contrast in STEM ADF imaging of amorphous solids (Gibson & Howie 1978–9). However, the nature of transverse and z-incoherence effects in the context of imaging perfect crystals at atomic resolution was not specifically addressed.

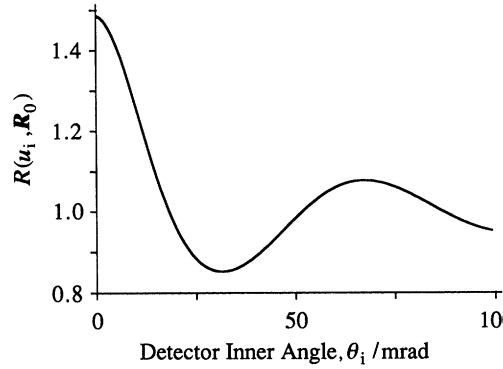

Figure 8. Ratio of the ADF signal to the incoherent signal as a function of θ_i for two silicon columns separated by 0.5 Å. The 2.2 Å (FWHM) probe is over the centre of the dumbbell at a defocus of −70 nm. The convergence angle is 10.3 mrad and $C_s = 1.3$ mm.

5. z-coherence: higher-order terms

In the previous sections, we have shown that a Howie detector function $D^{\mathrm{H}}(\boldsymbol{u})$ cannot eliminate interference effects between atoms in the same column of a crystal projection. It was found that a peak in the characteristic object function has a strength proportional to the square of the number of atoms in a column. However, this simple picture of in-phase z-coherence can often break down in cases of practical importance. It is seldom possible to ignore terms higher than $\sigma^2\phi^2(\boldsymbol{R})$ in the transmission function for a column of medium to heavy atoms. Then, dynamical effects cause the scattering from individual atoms in the column to add in a highly nonlinear fashion. In this section, we specifically consider the effect of these higher-order terms and establish the important result that transverse incoherent imaging is unaffected in the case of strong phase objects.

To extend the analysis of §2 to the case of a strong phase object, it is necessary to consider higher-order terms in the expansion of the transmission function $t(\boldsymbol{R})$ where

$$t(\boldsymbol{R}) = \exp(-\mathrm{i}\sigma\phi(\boldsymbol{R})). \tag{35}$$

It is convenient to rewrite (35) in the form

$$t(\boldsymbol{R}) = 1 - \mathrm{i}\sigma U(\boldsymbol{R}), \tag{36}$$

where $U(\boldsymbol{R})$ is the dynamical pseudo-potential

$$U(\boldsymbol{R}) = (1/\mathrm{i}\sigma)[(\mathrm{i}\sigma\phi(\boldsymbol{R})) - \tfrac{1}{2}(\mathrm{i}\sigma\phi(\boldsymbol{R}))^2 + \tfrac{1}{6}(\mathrm{i}\sigma\phi(\boldsymbol{R}))^3 - \ldots]. \tag{37}$$

Thus it is always possible to reduce a strong phase object to a single scattering 'pseudo-object' described by the potential $U(\boldsymbol{R})$. The fact that $U(\boldsymbol{R})$ is complex directly implies the breakdown of Friedel's Law for a non-centric crystal projection in the presence of multiple scattering. It can be seen from (37) that all of the terms in $U(\boldsymbol{R})$ are sharply peaked about the projected atom positions. The real space arguments of §2 can therefore be applied to each successive term to give an expression identical to (23);

$$I(\boldsymbol{R}_0) = P^2(\boldsymbol{R}_0) * O^s(\boldsymbol{R}_0) \tag{38}$$

but with the strong phase object function $O^s(\boldsymbol{R})$ given by

$$O^s(\boldsymbol{R}) = |[(\mathrm{i}\sigma\phi(\boldsymbol{R})) - \tfrac{1}{2}(\mathrm{i}\sigma\phi(\boldsymbol{R}))^2 + \tfrac{1}{6}(\mathrm{i}\sigma\phi(\boldsymbol{R}))^3 - \ldots] * d(\boldsymbol{R})|^2. \tag{39}$$

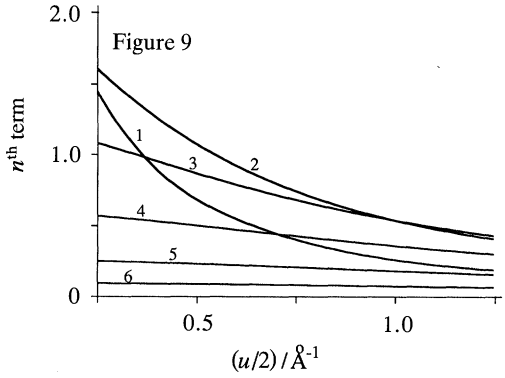

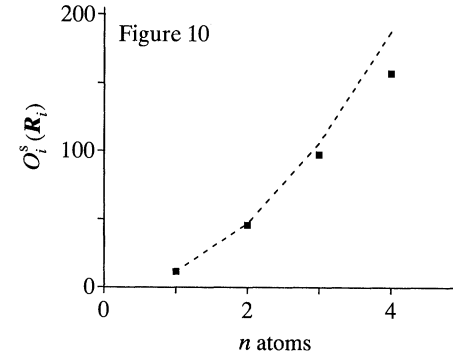

Figure 9. Higher-order multiple scattering terms of the object function (equation (42)) for a column of three uranium atoms plotted against scattering angle at 40 kV.

Figure 10. Columnar object function (equation (42)) calculated for n uranium atoms at 40 kV and a 30 mrad inner detector angle. The dashed line shows the ideal in-phase coherent n^2 dependence extrapolated from the $n = 1$ value.

For a low-index crystal projection, we now express $\phi(\boldsymbol{R})$ in terms of the projected atomic contributions $\phi_i(\boldsymbol{R}-\boldsymbol{R}_i)$ so that under incoherent imaging conditions (equations (22) and (25)),

$$O^s(\boldsymbol{R}) = \sum_{\boldsymbol{R}_i} O_i^s(\boldsymbol{R}-\boldsymbol{R}_i), \tag{40}$$

where

$$O_i^s(\boldsymbol{R}) = |[(\mathrm{i}n_i\,\sigma\phi_i(\boldsymbol{R}))-\tfrac{1}{2}(\mathrm{i}n_i\,\sigma\phi_i(\boldsymbol{R}))^2+\tfrac{1}{6}(\mathrm{i}n_i\,\sigma\phi_i(\boldsymbol{R}))^3-\ldots]*d(\boldsymbol{R})|^2. \tag{41}$$

In the weighted delta function approximation, the equivalent of (27) is

$$O_i^s(\boldsymbol{R}_i) = \delta(\boldsymbol{R}-\boldsymbol{R}_i)\int |\mathrm{i}n_i\,\sigma\Phi_i(\boldsymbol{u})+\tfrac{1}{2}n_i^2\,\sigma^2\Phi_i(\boldsymbol{u})*\Phi_i(\boldsymbol{u}) -\tfrac{1}{6}\mathrm{i}n_i^3\,\sigma^3\Phi_i(\boldsymbol{u})*\Phi_i(\boldsymbol{u})*\Phi_i(\boldsymbol{u})-\ldots|^2 D^{\mathrm{H}}(\boldsymbol{u})\,\mathrm{d}\boldsymbol{u}, \tag{42}$$

which is analogous to the use of complex scattering factors for single atoms (Zeitler & Olsen 1967). Here $\Phi_i(\boldsymbol{u})$ is the ith atom scattering factor calculated in the first Born approximation and expressible as a sum of gaussians (Doyle & Turner 1968);

$$\Phi_i(\boldsymbol{u}) = \sum_{j=1,4} a_j \exp(-b_j s^2). \tag{43}$$

The convolutions contained in (42) can therefore be evaluated analytically so that the third term, for example, may be written as a sum of gaussians in reciprocal space;

$$\Phi_i(\boldsymbol{u})*\Phi_i(\boldsymbol{u})*\Phi_i(\boldsymbol{u}) = \sum_{l,j,k-1,4} a_l\,a_j\,a_k \frac{\pi}{b_l\,b_j+b_l\,b_k+b_j\,b_k} \times\exp\left\{-\left(\frac{b_l\,b_j\,b_k}{b_l\,b_j+b_l\,b_k+b_j\,b_k}\right)s^2\right\}. \tag{44}$$

The higher-order scattering terms will have different widths and will each assume a greater importance in different regions of reciprocal space. This is illustrated in figure 9 for a column comprising three uranium atoms at 40 kV. This situation is directly relevant to the impressive imaging experiments of Isaacson and coworkers (see fig.

13.9 of Isaacson *et al.* (1979)) which clearly show the resolved columns of a uranium microcrystal. This image was interpreted entirely using incoherent imaging theory. Although this is largely justified in the transverse direction because in this case $\theta_i \approx 1.22\lambda/\Delta R$ (equation (33)), the calculated columnar object function in figure 10 suggests that the intensity will increase approximately as the number of atoms in the column squared. Thus, it would seem inappropriate to consider the columnar intensity as resulting from an incoherent sum of contributions from the atoms contained within the column. In particular, a single atom will appear a factor of 4 fainter than two atoms with the same projected coordinate so it would be quite possible to misinterpret such weak features in the image. We believe this might be the case for the uranium microcrystal image mentioned above where the weakest spots in the image probably represent single atoms or monolayer rafts. Ignoring this intensity level would then explain the apparent linear imaging observed by Isaacson *et al.* (1979) since n^2 increases roughly linearly between $n = 2$ and 4. The apparent reduction in the calculated signal of figure 10 compared with the n^2 dependence of 'ideal' in phase coherent scattering can be directly attributed to multiple scattering. Increasing the number of atoms in the column implicates higher-order terms in the expansion (equation (41)) and broadens the overall scattering distribution. Indeed, the form of equations (42) and (44) suggest that it might be possible to tabulate a parametric fit to the strong phase object function in a manner analogous to atomic scattering factor work (Doyle & Turner 1968; Molière 1947; Pennycook *et al.* 1986; Zeitler & Olsen 1964). However, since the Howie detector averages over several multiple scattering terms, the deviations away from the n^2 behaviour are remarkably small suggesting that images can be interpreted intuitively without the need for complicated image simulation. This is a significant advantage of this imaging mode and has important implications for the study of very thin specimens in many areas of materials science.

6. Beyond the phase object approximation

In this section, we explore how the imaging process is affected when Fresnel diffraction becomes important and the convenient assumption of a perfect phase object breaks down. We use a simple but illuminating analytical approach which has some validity for large-angle scattering and is similar to the concept of a thick phase grating introduced by Cowley & Moodie (1962).

As discussed in §2, a thickness limit exists for scattering to an angle θ beyond which the POA becomes inappropriate and the atoms within the column can no longer be regarded as scattering perfectly in phase. In kinematic theory, for a semi-infinite slab of finite thickness t, it is customary to describe columnar defocusing effects by the well-known shape transform

$$s(\boldsymbol{u}) = \int_0^t \exp(-2\pi i s_u z)\,\mathrm{d}z, \tag{45}$$

where s_u is the deviation parameter between the scattering vector $\boldsymbol{u}$ and the Ewald sphere construction for an incident electron wavevector k of transverse component $\boldsymbol{K}$;

$$s_u = (1/2k)(2\boldsymbol{K}\cdot\boldsymbol{u} - u^2). \tag{46}$$

We now make the large-angle scattering assumption $u \gg K$ giving

$$s_u \approx -u^2/2k. \tag{47}$$

Physically, this means that at large enough scattering angles, z-defocusing is dominated by the curvature of the Ewald sphere. Incorporating this phase change directly into (15) then gives a modified large-angle single scattering result;

$$I(\boldsymbol{R}_{\mathrm{o}}) = \sigma^2 \int |[\Phi(\boldsymbol{u}) * A(\boldsymbol{u}) \exp(\mathrm{i}\chi(\boldsymbol{u}) + 2\pi \mathrm{i}\boldsymbol{u}\cdot\boldsymbol{R}_{\mathrm{o}})] S^{\mathrm{H}}(\boldsymbol{u})|^2 D^{\mathrm{H}}(\boldsymbol{u})\,\mathrm{d}\boldsymbol{u}, \tag{48}$$

where $S^{\mathrm{H}}(\boldsymbol{u})$ is the high-angle shape transform

$$S^{\mathrm{H}}(\boldsymbol{u}) = \int_0^t \exp(\mathrm{i}\pi u^2 z/k)\,\mathrm{d}z \tag{49}$$

and $\Phi(\boldsymbol{u})$ now represents the reciprocal space structure amplitude per unit slice (i.e. the Fourier transform of the projected potential of one slice of the crystal). We emphasize that incorporating the shape transform in this way is only valid for a large inner-angle Howie detector. Following the real space arguments of §2 then gives

$$I(\boldsymbol{R}_{\mathrm{o}}) = P^2(\boldsymbol{R}_{\mathrm{o}}) * O^z(\boldsymbol{R}_{\mathrm{o}}, t), \tag{50}$$

where $O^z(\boldsymbol{R}, t)$ is now a thickness dependent object function

$$O^z(\boldsymbol{R}, t) = \sigma^2 \sum_{\boldsymbol{R}_j} O_j^z(\boldsymbol{R} - \boldsymbol{R}_j) \tag{51}$$

and

$$O_j^z(\boldsymbol{R}) = |\phi_j^z(\boldsymbol{R}) * S^{\mathrm{H}}(\boldsymbol{R}, t) * d(\boldsymbol{R})|^2 \tag{52}$$

is the z-defocused object function for the jth column 'slice' potential $\phi_j^z(\boldsymbol{R}) = n_j \phi_j(R)/t$. Here,

$$S^{\mathrm{H}}(\boldsymbol{R}, t) = \frac{\mathrm{i}}{\lambda} \int_0^t \exp\left(-\frac{\mathrm{i}R^2}{2\lambda z}\right) \mathrm{d}z \tag{53}$$

is the Fresnel propagator function integrated along the column. Thus, transverse incoherent imaging is still obtained in a large-angle single scattering approximation. However, the object function is now a function of thickness depending on the defocusing effects of atoms located at different heights in the column. A special case of (53) involves two isolated atoms with the same projected coordinate $\boldsymbol{R}_i$ but separated by a distance Δz. The curvature of the Ewald sphere over the angular range of the ADF detector means that coherence will be destroyed if $\Delta z \gg k/(u_{\mathrm{e}}^2 - u_{\mathrm{i}}^2)$ where u_{e} defines the effective outer detector angle which in practice is governed by the fall off in atomic scattering factors. For typical conditions of $u_{\mathrm{i}} = 1.08$ Å^{-1} ($\theta_{\mathrm{i}} =$ 40 mrad), $u_{\mathrm{e}} = 1.62$ Å^{-1} ($\theta_{\mathrm{e}} = 60$ mrad) and 100 kV electrons, we have $\Delta z \gg 20$ Å which agrees with similar conclusions by Gibson & Howie (1978–79) and Fertig & Rose (1977). Clearly, the Howie detector is considerably less efficient at destroying coherence in the z-direction compared with the transverse plane. For an atomic column, the typical interatomic spacings are small and interference effects along the column must be included explicitly using (53). Consider, for example, the projected potential of figure 6 assuming the columns to consist of Si atoms spaced at 4 Å. The Fresnel interference effects between atoms in the column manifest themselves as radial fringes in the full kinematic simulation contained in figure 11 which supports the large-angle scattering assumption, equation (47). The vertical bands of intensity correspond to the transverse coherence effects discussed in §2, but the radial fringes resulting from z-coherence scale the intensity in a highly nonlinear fashion. More specifically, the signal oscillates about a mean value with increasing thickness due to the bright inner fringe building up intensity and then falling off the detector. This is

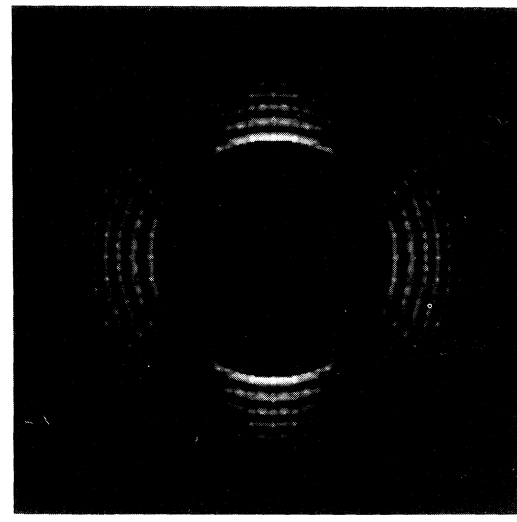

Figure 11. CBED pattern simulation for the projected potential of figure 6 with the probe located over a dumbbell. The kinematic calculation includes z-defocusing effects explicitly for a 10 nm thick crystal and a 50 mrad inner detector angle. Other imaging conditions are identical to figure 7a.

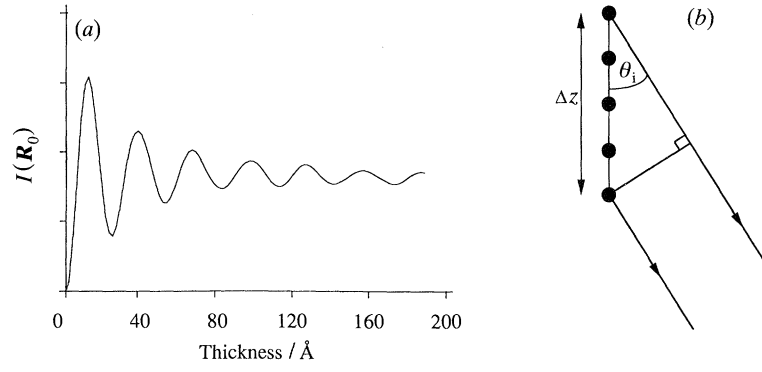

Figure 12. (a) Image intensity as a function of specimen thickness for Si[110] at 100 kV. The 2.2 Å (FWHM) probe is located over a dumbbell (see figure 13c) and the detector angular range is 50–150 mrad. The probe convergence angle is 10.3 mrad, and $C_s = 1.3$ mm. Interference effects between atoms at different heights in the crystal are included explicitly. (b) Real space scattering geometry for a column of atoms.

further illustrated by the calculation for Si[110] as displayed in figure 12a. We assume a 50–150 mrad annular detector with a 2.2 Å (FWHM) probe located over the centre of a dumbbell (see figure 13). The relevant detected portion of the zero-layer CBED pattern is displayed in figure 13a. The initial part of the curve in figure 12a increases for small t as the number of atoms squared, but z-coherence effects rapidly suppress the high-angle signal at around 1 nm. A simple real space interpretation of this thickness dependence is illustrated in figure 12b. Assuming that the ADF signal is dominated by scattering which is close to the inner periphery of the detector at angle θ_i, destructive interference will occur for a column length of $\Delta z = 2\lambda/\theta_i^2$. This is equal to about 3 nm for $\theta_i = 50$ mrad, which is in excellent agreement with the first minimum present in the full kinematic calculation of figure 12a. This explains why high-angle thermal diffuse scattering, which is effectively generated incoherently by

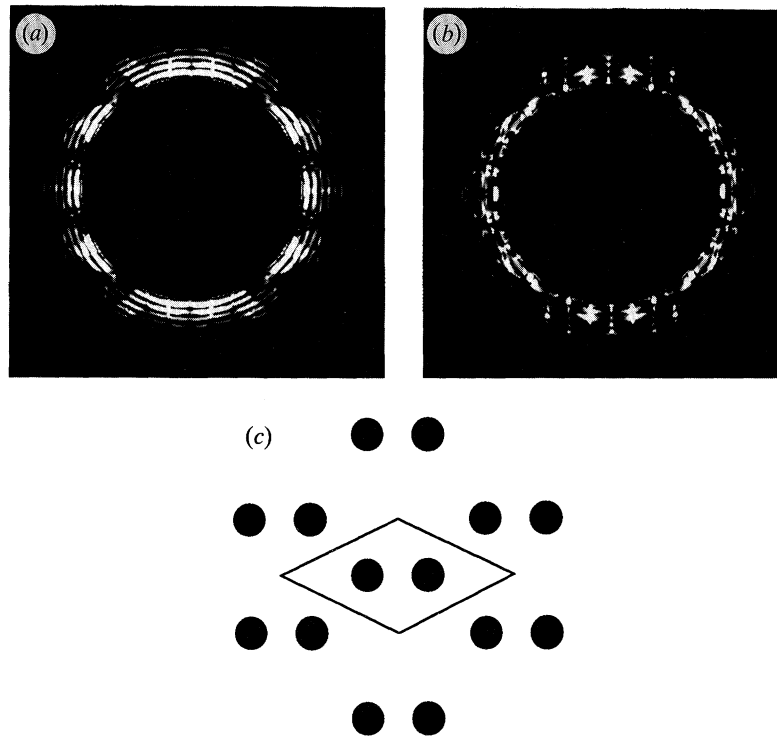

Figure 13. (*a*) Detected portion of a CBED pattern relevant to the calculation of figure 12. The probe is located over a dumbbell (*a*) and channel (*b*) of the Si[110] projection shown schematically in (*c*). The crystal thickness is 20 nm.

each slice of the crystal (Rez *et al.* 1977; Young & Rez 1975) quickly dominates in thicker crystals. In this case, z-incoherence is naturally built into the imaging process (Pennycook & Jesson 1990, 1991) even though this is impossible to achieve using coherently scattered electrons and a Howie detector.

Finally, for a thick phase grating we note that transverse incoherent imaging of the object function

$$O^T(\boldsymbol{R},t) = \sigma^2 \sum_{\boldsymbol{R}_j} O_j^T(\boldsymbol{R}-\boldsymbol{R}_j) \tag{54}$$

is also obtained where

$$O_j^T(\boldsymbol{R}) = |U_j^z(\boldsymbol{R}) * S^{\mathrm{H}}(\boldsymbol{R},t) * d(\boldsymbol{R})|^2 \tag{55}$$

is the object function for the jth column slice pseudo-potential

$$U_j^z(\boldsymbol{R}) = (1/\mathrm{i}\sigma)[(\mathrm{i}\sigma\phi_j^z(\boldsymbol{R})) - \tfrac{1}{2}(\mathrm{i}\sigma\phi_j^z(\boldsymbol{R}))^2 + \tfrac{1}{6}(\mathrm{i}\sigma\phi_j^z(\boldsymbol{R}))^3 - \ldots]. \tag{56}$$

This result takes into account both multiple scattering and Fresnel diffraction effects and is valid to crystal thicknesses where the two effects can be treated separately. The implications of this analysis should therefore be at least qualitatively representative of multislice simulations of high-angle ADF STEM images formed from coherently scattered electrons. Recently, several authors have performed such calculations and have been surprised by the apparent close agreement with incoherent imaging theory (Xu *et al.* 1990; Wang & Cowley 1989, 1990; Shin *et al.* 1989). Clearly, this is just a manifestation of the transverse incoherence effects suggested by (50)–(56). Note that our discussion of coherent scattering from 3D

objects has not specifically addressed the question of diffraction to higher-order Laue zones (HOLZs) of the reciprocal lattice. However, we believe that such reflections will be dominated by zero-layer scattering at small crystal thicknesses and will be rapidly dominated by incoherently generated thermally scattered electrons in thicker specimens (Pennycook & Jesson 1991).

7. Discussion

In this paper, we have shown how an incoherent image of a phase object can be formed by using coherently scattered electrons. A STEM equipped with a large inner angle Howie detector suppresses interference effects in the transverse plane of the phase object. This transverse incoherence lends itself to a real space interpretation which has important implications for intuitive imaging. By tuning the inner detector angle for a given imaging experiment, it should, therefore, be possible to obtain intuitive images of atomic clusters and monolayer rafts with an optimum signal-to-noise ratio.

The inability of the Howie detector to destroy z-coherence in a phase object has been discussed in §5. Atoms possessing the same projected coordinate $\boldsymbol{R}_{\mathrm{i}}$ will add in phase so that the signal will vary as the number of atoms squared. Images should therefore be interpreted accordingly. For strongly scattering columns, dynamical diffraction will further influence the n^2 dependence. It is, however, intriguing that this departure is quite small for the strong phase uranium column of figure 10. It would appear that the Howie detector averages several of the multiple scattering terms in (42) (see also figure 9) which reduces the sensitivity of the signal to a change in shape of the scattering distribution. This is most likely a general effect applicable to most situations of practical interest within the phase object régime.

8. Conclusions

Using a large inner angle ADF detector, we have shown how to overcome the 'hole-in-the-detector problem' which is the major obstacle preventing a simple interpretation of atomic resolution STEM images of thin specimens. It is only necessary to detect a representative fraction of the total scattered intensity to form an incoherent image of a phase object using coherently scattered electrons. This can be achieved if the inner radius of the annular detector is increased so that the detector function $d(\boldsymbol{R})$ is narrow compared with the dimensions of the probe (equation (22)). This mode conveys the advantages of incoherent imaging although scattering to the detector is governed by a coherent object function if projected atomic contributions overlap. In turn, this coherence can also be removed by further increasing the inner angle so that $d(\boldsymbol{R})$ is narrow compared with the atom separation (equation (25)). Incoherent imaging of a phase object where the atomic columns contribute independently is then achieved. The high-angle coherent signal is rapidly suppressed in three-dimensional (3D) objects by columnar defocusing and is replaced by incoherently generated thermal diffuse scattering. This effectively builds 3D incoherence into the imaging process.

We thank J. M. Cowley, J. M. Gibson, and J. Silcox for stimulating our interest in STEM ADF imaging of very thin specimens and S. L. Carney, T. C. Estes, and J. T. Luck for technical assistance. This work was sponsored by the Division of Materials Science, U.S. Department of Energy, under Contract DE-AC05-84OR21400 with Martin Marietta Energy Systems, Inc.

References

Ade, G. 1977 *Optik* **49**, 113–116.

Born, M. & Wolf, E. 1980 *Principles of optics*. Pergamon Press.

Colliex, C. & Mory, C. 1983 *Quantitative electron microscopy* (ed. J. N. Chapman & A. J. Craven), pp. 149–216. SUSSP.

Cowley, J. M. & Moodie, A. F. 1962 *J. Phys. Soc. Jap.* **17** (Suppl. BII), 86.

Cowley, J. M. 1976 *Ultramicroscopy* **2**, 3–16.

Cowley, J. M. 1986 *Principles of analytical electron microscopy* (ed. D. C. Joy, A. D. Romig Jr & J. I. Goldstein), pp. 77–122. New York: Plenum Press.

Cowley, J. M. 1988 *High resolution transmission electron microscopy* (ed. P. R. Buseck, J. M. Cowley & L. Eyring), pp. 38–57. Oxford University Press.

Crewe, A. V. 1970 *Q. Rev. Biophys.* **3**, 137–179.

Crewe, A. V. & Wall, J. 1970 *Optik* **30**, 461–474.

Doyle, P. A. & Turner, P. S. 1968 *Acta crystallogr.* A **43**, 390–397.

Engel, A. 1974 *Optik* **41**, 117–126.

Engel, A., Wiggins, J. W. & Woodruff, D. C. 1974 *J. appl. Phys.* **45**, 2739–2746.

Fertig, J. & Rose, H. 1977 *Ultramicroscopy* **2**, 269–279.

Gibson, J. M. & Howie, A. 1978–79 *Chem. Scr.* **14**, 109–116.

Goodman, J. W. 1968 *Introduction to Fourier optics*, p. 109. New York: McGraw-Hill.

Hall, C. R. 1965 *Phil. Mag.* **12**, 815–826.

Howie, A. 1979 *J. Micros.* **117**, 11–23.

Isaacson, M., Ohtsuki, M. & Utlaut, M. 1979 *Introduction to analytical electron microscopy* (ed. J. J. Hren, J. Goldstein & D. C. Joy), pp. 343–368. New York and London: Plenum Press.

Jesson, D. E. & Pennycook, S. J. 1990 *Electron Microscopy 1990, Proc. 12th Int. Cong. Electron Microsc. vol. 1: Imaging Sciences* (ed. L. D. Peachey & D. B. Williams), pp. 74–75. San Francisco Press.

Jesson, D. E., Pennycook, S. J. & Baribeau, J.-M. 1991 *Phys. Rev. Lett.* **66**, 750–753.

Jesson, D. E., Pennycook, S. J., Baribeau, J.-M. & Houghton, D. C. 1992 *Phys. Rev. Lett.* **68**, 2062–2065.

Molière, G. 1947 *Z. Naturforsch.* **2a**, 133–145.

Pennycook, S. J., Berger, S. D. & Culbertson, R. J. 1986 *J. Microsc.* **144**, 229–249.

Pennycook, S. J. & Jesson, D. E. 1990 *Phys. Rev. Lett.* **64**, 938–941.

Pennycook, S. J. & Jesson, D. E. 1991 *Ultramicroscopy* **37**, 14–38.

Pennycook, S. J., Chisholm, M. F., Jesson, D. E., Norton, D. P., Lowndes, D. H., Feenstra, R., Kerchner, H. R. & Thomson, J. O. 1991 *Phys. Rev. Lett.* **67**, 765–768.

Rez, P., Humphreys, C. J. & Whelan, M. J. 1977 *Phil. Mag.* **35**, 81–96.

Scherzer, O. 1949 *J. appl. Phys.* **20**, 20–29.

Shin, D. H., Kirkland, E. J. & Silcox, J. 1989 *Appl. Phys. Lett.* **55**, 2456–2458.

Spence, J. C. H. & Cowley, J. M. 1978 *Optik* **50**, 129–142.

Wall, J., Langmore, J., Isaacson, M. & Crewe, A. V. 1974 *Proc. natn. Acad. Sci. USA* **71**, 1–5.

Wang, Z. L. & Cowley, J. M. 1989 *Ultramicroscopy* **31**, 437–453.

Wang, Z. L. & Cowley, J. M. 1990 *Ultramicroscopy* **32**, 275–289.

Xu, P., Kirkland, E. J., Silcox, J. & Keyse, R. 1990 *Ultramicroscopy* **32**, 93–102.

Young, A. P. & Rez, R. 1975 *J. Phys.* C **8**, L1–L7.

Zeitler, E. & Olsen, H. 1964 *Phys. Rev.* **136**, 1546–1552.

Zeitler, E. & Olsen, H. 1967 *Phys. Rev.* **162**, 1439–1447.

Zeitler, E. & Thomson, M. G. R. 1970 *Optik* **31**, 258–280.

Received 25 February 1992; revised 8 June 1992; accepted 31 July 1992